



Mid-infrared three-states nanoimaging of reconfigurable binary chalcogenide Sb_2S_3

Ming-Jyun Ye^{a,b}, Ilario Bisignano^b, Ross Y.M. Wong^b, Hung-Wen Chen^c, Yoshihiko Takeda^d, Kuo-Ping Chen^{c,*}, Satoshi Ishii^{b,*}

^a College of Photonics, National Yang Ming Chiao Tung University, Tainan, Taiwan

^b Research Center for Materials Nanoarchitectonics (MANA), National Institute for Materials Science (NIMS), Tsukuba, Japan

^c Institute of Photonics Technologies, National Tsing Hua University, Hsinchu, Taiwan

^d Research Center for Energy and Environmental Materials, National Institute for Materials Science (NIMS), Tsukuba, Japan

ARTICLE INFO

Keywords:

Phase change material
Binary chalcogenide
Antimony sulfide
Near-field optical microscopy
Nano-FTIR

ABSTRACT

Conventional ternary chalcogenide phase change materials (PCMs) have been widely used for near-infrared to mid-infrared applications but typically exhibit only two phases. In contrast, antimony sulfide (Sb_2S_3) is a binary phase-change material that can take three states and consists of earth-abundant elements. Despite its potential as a new class of PCM, Sb_2S_3 remains relatively underexplored. In the current work, we employ Raman spectroscopy and nano-FTIR to investigate phase transitions of Sb_2S_3 induced by femtosecond-pulsed and continuous-wave lasers. In particular, nano-FTIR enables nanoscale characterization of reversible phase transitions and clear identification of the typically elusive intermediate state. By integrating nano-FTIR and Raman spectroscopy, we correlate morphological and chemical features with optical responses. Crucially, the nano-FTIR amplitude distributions under broadband excitation are governed not only by the magnitude of the dielectric constant but also by the sensing depths. This work advances the understanding and application of binary chalcogenide PCMs for mid-infrared photonic devices.

Introduction

Phase change materials (PCMs) offer a promising approach for reconfiguring optical properties via external energy stimuli, such as annealing, pulse laser, or electrical short pulse. Utilizing electrical [1] or laser-induced [2] switching, the active programmable metasurfaces and optical photonics are investigated. Combining ultra-thin film (below 55 nm) PCMs and polar substrates has gained attention in recent years. Nonvolatile germanium-antimony-tellurium ($\text{Ge}_3\text{Sb}_2\text{Te}_6$ or $\text{Ge}_1\text{Sb}_2\text{Te}_4$), sometimes with polar substrates, is systematically explored from mid-infrared (mid-IR) to the far-IR range [3–6]. Nonvolatile PCMs' natural properties contribute to reducing low energy consumption and stability, making PCM-based devices highly appealing from a green technology perspective. However, achieving precise control over metal composition (e.g., Te-rich or Ge-rich) and ensuring homogeneity in ternary materials, such as GeSbTe alloys, presents several inherent challenges [7–9].

Recently, the binary chalcogenide antimony sulfide (Sb_2S_3) has garnered significant attention for its advantages over GeSbTe , including

its earth abundance and low optical loss in the visible. A characteristic nature of Sb_2S_3 against GeSbTe is its ability to form intermediate states between crystalline and amorphous states. The intermediate state is a mixture of crystalline and amorphous states, as identified by others [10, 11]. Sb_2S_3 has been explored for various applications such as programmable metasurfaces [2,12], nanophotonic devices [13], and silicon photonics [1], spanning from the visible to the NIR spectrum. However, in the mid-infrared (mid-IR) range, research has primarily focused on chemically synthesized Sb_2S_3 components doped with rare elements [14,15].

Notably, there is a scarcity of studies on nanoscale mid-IR spectroscopy of Sb_2S_3 that demonstrate reconfigurable states. Nano-FTIR is a variant of scattering-type near-field scanning optical microscopy (s-NSOM) that integrates a broadband infrared illumination and interferometric detection for Fourier transform spectroscopy [16,17]. Unlike conventional s-NSOM, which typically operates at single or a few discrete wavelengths, nano-FTIR records a broad infrared spectrum. This approach enables acquisition of infrared spectra with nanoscale spatial resolution, enabling detailed chemical and structural

* Corresponding authors.

E-mail addresses: kpchen@ee.nthu.edu.tw (K.-P. Chen), sishii@nims.go.jp (S. Ishii).

<https://doi.org/10.1016/j.apsadv.2026.101000>

Received 15 October 2025; Received in revised form 11 April 2026; Accepted 30 April 2026

Available online 13 May 2026

2666-5239/© 2026 The Authors. Published by Elsevier B.V. This is an open access article under the CC BY-NC license (<http://creativecommons.org/licenses/by-nc/4.0/>).

characterization of phase change processes at the nanoscale.

In this work, we optically investigate Sb_2S_3 associated with the amorphization and crystallization laser irradiation. We analyze the three distinct states of Sb_2S_3 using Raman spectroscopy and nano-FTIR following femtosecond laser-induced amorphization and continuous-wave (CW) laser crystallization. In particular, the nanoscale optical insights from nano-FTIR imaging provide strong evidence to advance next-generation technologies, including high-density optical memory systems and thermography applications in unmanned vehicles, surveillance systems, and astronomy.

Results and discussion

The transition from crystalline to amorphous and the reverse process can be accomplished using femtosecond pulses and CW lasers, respectively. Generally, amorphization occurs through a melt-quench process that involves heating the PCMs to high temperatures (above the melting point) to melt them, followed by a short heating period to ensure rapid cooling and prevent recrystallization, shown in Fig. 1(a). Crystallization requires a longer heating time at moderately high temperatures (below the melting point) to promote crystal formation and growth [18]. In Fig. 1(b), the permittivities of amorphous and crystalline Sb_2S_3 collected by ellipsometry are shown. The solid lines represent the real parts of the dielectric functions (ϵ_1) for amorphous (a-) and crystalline (c-) Sb_2S_3 , with values of around 6 and 10, respectively. The dashed lines correspond to the imaginary part of the dielectric function (ϵ_2) for a- and c- Sb_2S_3 . In Fig. 1(c), the simulated second-order amplitude (O2A) spectra of nano-FTIR following the model [19] with a 10-nm ITO thin film between the Sb_2S_3 and substrate are shown. It is anticipated that the two phases are distinguishable by nano-FTIR. Note that, as shown in Figure S1, the existence of a 10-nm ITO thin film only affects the slight shifts in the magnitude of the spectra. Additionally, around a 10 nm thickness decrease, which could happen in the amorphization process as discussed later, does not affect the trend of O2A spectra for a- and c- Sb_2S_3 as shown in Figure S1. While the crystal and amorphous phases

of Sb_2S_3 are well known, an additional intermediate state has not been investigated intensively except in a few studies [1,10], and thus identifying the intermediate state is the major focus of this work.

Sb_2S_3 amorphization process by femtosecond laser (crystalline, intermediate-crystalline, and fully quenched amorphous)

The fabrication of Sb_2S_3 thin films began with the deposition of a- Sb_2S_3 on an ITO/glass substrate by e-beam evaporation. Following this, the sample was annealed in vacuum after depositing a 15 nm protective SiO_2 layer by e-beam evaporation. A protective layer helps prevent thickness changes [1,20]. As noted in our previous paper, the absence of a protective layer results in a reduced Sb_2S_3 thickness [13]. Lastly, the amorphization process was achieved via pulsed laser irradiation, resulting in both intermediate-crystalline and fully quenched amorphous Sb_2S_3 (denoted as IC and FQ), as illustrated in Fig. 2(b). The detailed parameters of the femtosecond pulse laser and the CW laser are shown in the Methods Section. The laser created a spatial gradient in which the high-intensity center melts and quenches into an amorphous state, while the lower-intensity periphery retains partial crystallinity in intermediate states, as illustrated in Fig. 2(b). The intermediate state was proved in both amorphization and crystallization.

Despite its relevance, the Raman characterization of locally reversible Sb_2S_3 during amorphization and subsequent crystallization has not been comprehensively investigated. When performing Raman spectroscopy, it should be noted that Sb_2S_3 exhibits high absorption in the amorphous phase below 650 nm and in the crystalline phase below 700 nm [13]. Within the absorbing wavelength range, the phase change from IC or FQ to the crystalline state can be induced during Raman spectroscopy measurement. Therefore, to avoid phase change during Raman spectroscopy, a 785 nm CW laser was selected as the excitation source. The laser beam diameter on the sample was 4.5 μm , as shown in Figure S2. Fig. 2(c) shows the Raman features of crystalline Sb_2S_3 appear at 195, 235, 280, and 309 cm^{-1} (yellow dashed line). They show Sb-S stretching modes in the orthorhombic phase. The gray line at 149 cm^{-1} shows metallic Sb phase, and the peak corresponding to Sb_2O_3 is at 115 cm^{-1} [13,20–23]. Utilizing pulse laser irradiation, both IC and FQ Sb_2S_3

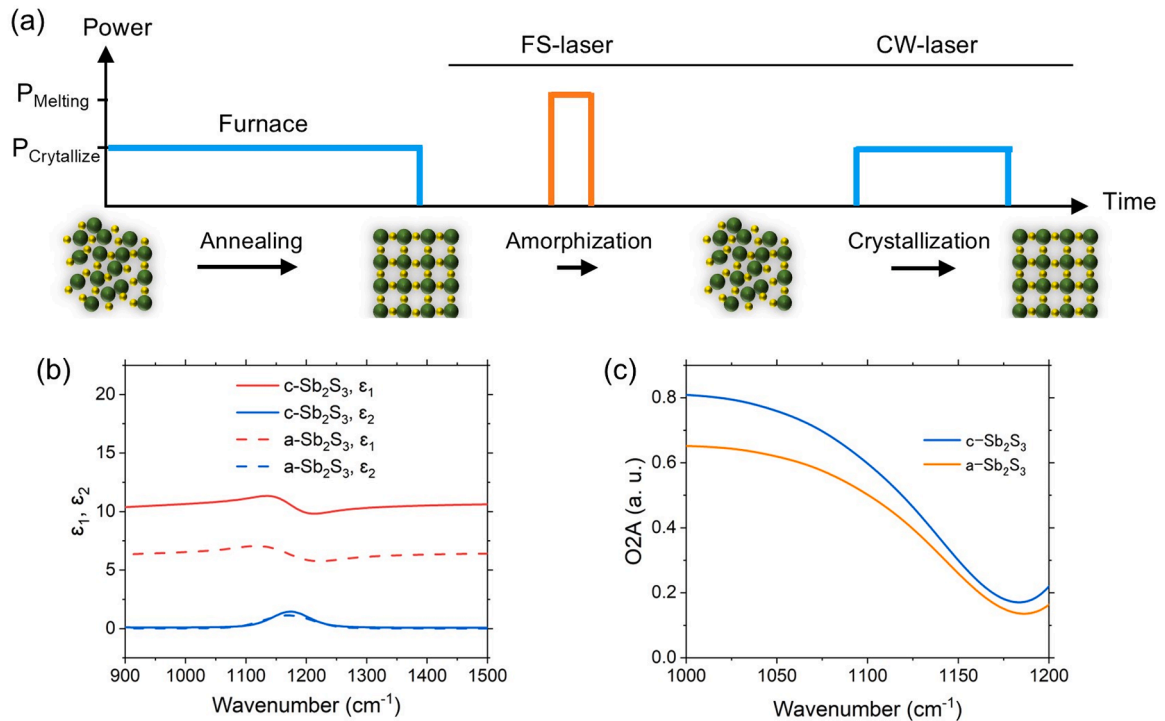


Fig. 1. (a) Schematic of Sb_2S_3 optical switching concept with a femtosecond (FS) and a CW lasers. (b) Permittivity of a- Sb_2S_3 and c- Sb_2S_3 . Red and blue colors represent the real and imaginary parts, respectively. (c) Calculated O2A spectra of nano-FTIR for the 150 nm Sb_2S_3 thin film on the ITO/glass substrate, where the orange and blue show a- Sb_2S_3 , and c- Sb_2S_3 , respectively.

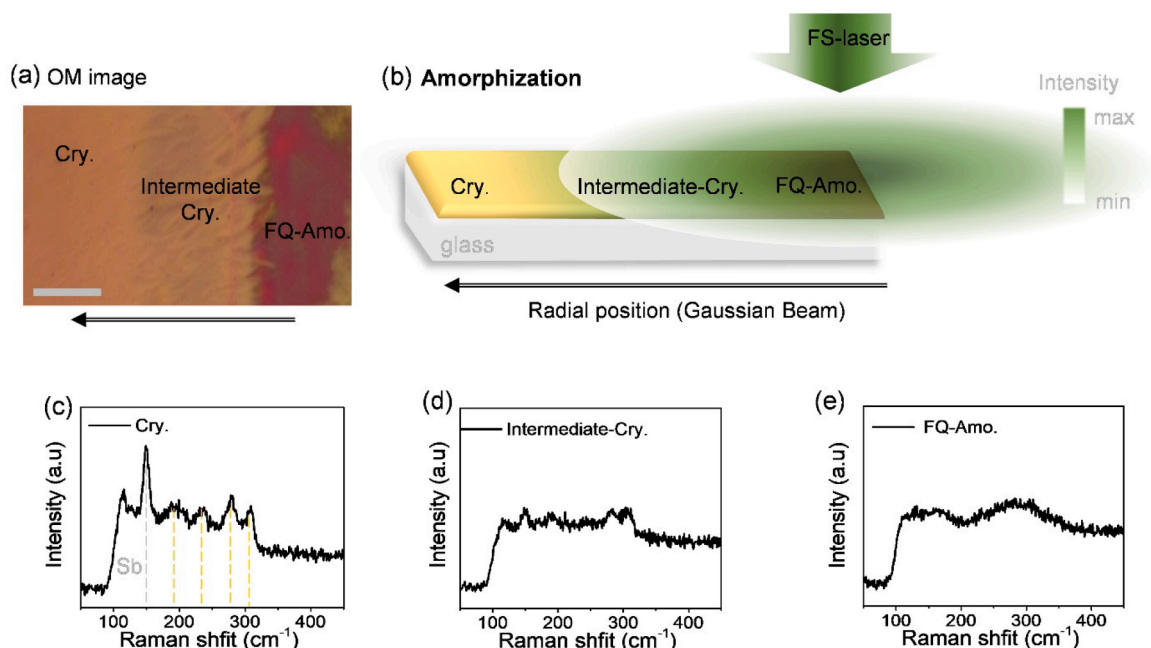


Fig. 2. (a) Optical microscope image of the Sb_2S_3 thin film after the laser quenching process. An arrow shows the radial position of the laser whose intensity decreases. Scale bar is 5 μm . (b) Schematic of femtosecond (FS) pulsed-laser-induced melting-quenched process with a Gaussian beam irradiated on the device. Raman spectra of Sb_2S_3 in (c) crystalline (Cry.), (d) intermediate-crystalline (Intermediate-Cry.), and (e) fully-quenched (FQ-Amo.) states.

were formed due to the Gaussian intensity distribution of the laser. As the laser intensity was weaker at the perimeter, in Fig. 2(d), the major peaks of crystalline Sb_2S_3 are still detectable but with lower intensity for the IC. The Raman spectrum for the FQ is shown in Fig. 2(e), showing broad features. Other leaf-like profiles of crystalline Sb_2S_3 Raman are shown in Figures S3 and S4. In the experiment, with the SiO_2 protecting layer, the Raman measurements didn't show major ablation and oxidation peak (e.g. Sb_2O_3) in the Sb_2S_3 .

In Fig. 3, the three states (crystalline, IC and FQ) of the Sb_2S_3 films were investigated via the nano-FTIR with a broadband laser covering 500–1500 cm^{-1} range. To normalize the spectrum, a silicon wafer was

used as the reference for all the nano-FTIR results. In the optical microscope image shown in Fig. 3(a), the measured area is enclosed by a black dashed frame. The irradiation region, located at the center of the frame, appears pink in color, with sawtooth patterns along the edges. Similar to the optical microscope image, the atomic force microscopy (AFM) image shown in Fig. 3(b) classifies the three states. While FQ Sb_2S_3 has a smooth and no crystal texture, IC and crystalline Sb_2S_3 have a leaf-like texture. Figs. 3(c) and 3(d) display second and third-order optical amplitudes (O2A and O3A) of the nano-FTIR. In general, the results indicate that amplitude increases with crystallinity, which correlates with permittivity. However, O2A contains signals from deeper

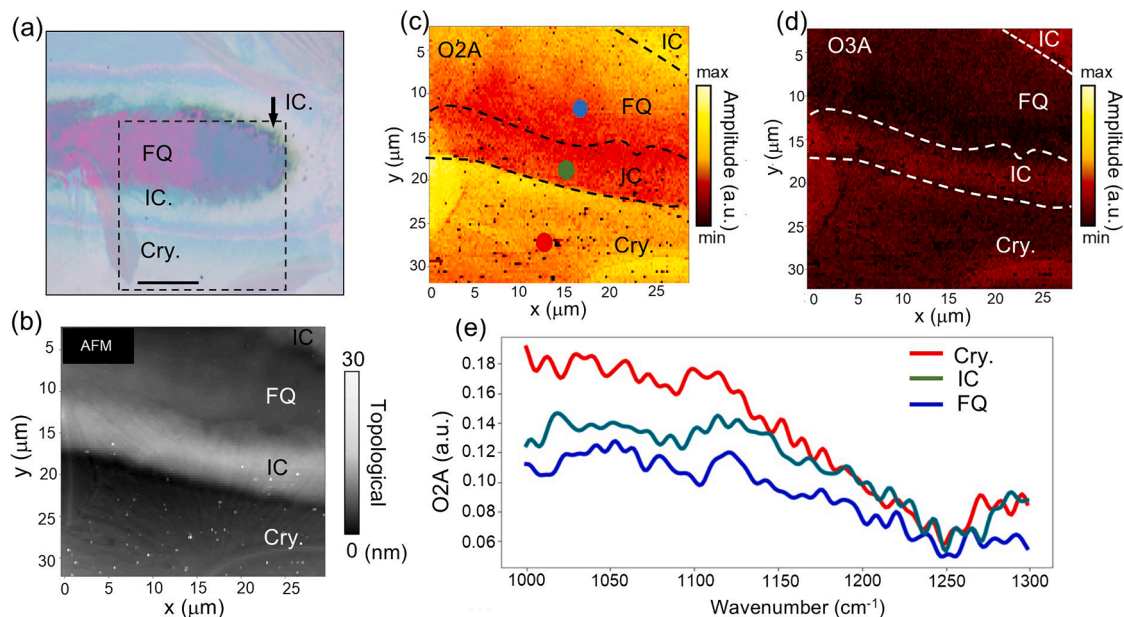


Fig. 3. (a) Optical microscope image of the Sb_2S_3 film where the laser beam irradiated. The scale bar is 10 μm . (b) Topography of the area surrounded by the black dashed frame in panel (a). Nano-FTIR mapping with an infrared broadband laser (500–1500 cm^{-1}) for the Sb_2S_3 sample showing (c) second-order amplitude (O2A) and (d) third-order amplitude (O3A). (e) Nano-FTIR spectra of the Sb_2S_3 in three different states.

regions than O3A [24]. Thus, in the O2A shown in Figure 3(c), some FQ areas are brighter than the IC area because the FQ area is slightly thinner than the IC area and the signal from the substrate is contributing. Similarly, the O3A image shown in Fig. 3(d) does not completely distinguish between the three states by amplitude. It is noted that a highly precise and controllable laser system has been used to analyze the intermediate states of the Sb_2S_3 [10], but without performing infrared spectroscopy. Figure 3(e) plots the O2A spectra, where the measured locations are indicated in Fig. 3(c) with the same color. Overall, c- Sb_2S_3 (red) has the largest amplitude, corresponding to the highest permittivity among the three states, followed by IC (green) and fully quenched (blue) Sb_2S_3 . Note that this result may differ if other positions are selected, such as the left boundary or the bottom right in Fig. 3(c). Also, as mentioned earlier in Figure S1, although there is a ~ 10 nm change in thickness in the IC and FQ areas from Fig. 3(b), this change has a negligible influence on the O2A. To summarize the above findings, the O2A intensity distribution among the three states is not entirely governed by the magnitude of the dielectric constant, and the same is true for O3A. Therefore, to avoid issues with morphology or variations in effective depth after irradiation, our proposed design concept should be implemented within a selected frequency range to demonstrate three distinct states, as explained in Fig. 4.

In Fig. 4(a), the scanning area of $5 \times 15.5 \mu\text{m}^2$ for the hyperspectral imaging was selected, marked with a white frame in the AFM image. The arrow indicates the line scan direction from FQ, IC, to the crystalline state. Hyperspectral imaging of the O2A with the wavenumber ranges limited to $900\text{--}1100 \text{ cm}^{-1}$, $1100\text{--}1200 \text{ cm}^{-1}$, and $1200\text{--}1300 \text{ cm}^{-1}$ are shown as Figs. 4(b), 4(c), and 4(d), respectively. In the $900\text{--}1100 \text{ cm}^{-1}$ range, the results reveal two distinct regions: crystalline and irradiated areas, which include IC and FQ. In the $1100\text{--}1200 \text{ cm}^{-1}$ range, the permittivity of Sb_2S_3 has strong wavenumber-dependence, such that the three states of Sb_2S_3 are distinguished, ordered from top to bottom: FQ, IC, and crystalline, each exhibiting well-defined edge boundaries. Compared to the former two images, the images in the range of $1200\text{--}1300 \text{ cm}^{-1}$ cannot distinguish the three states. A similar wavenumber-range dependence is also observed in the O3A images, as shown in Figure S5.

While Raman spectroscopy and nano-FTIR have been carried out to study chemical states of the samples, the visible reflectance spectra of three-state Sb_2S_3 after amorphization are demonstrated in Figure S6. The reflectance resonance dips start at 667 nm, 620 nm to 583 nm, corresponding to the Cry, IC, and FQ, respectively. These dips include changes in both refractive index and thickness. While Cry and IC states exhibit a vein-like appearance, the FQ state appears smooth. Thus, the reflectance spectra indicate that they can also be used to distinguish between different states.

Sb_2S_3 crystallization process by CW laser

In Fig. 5(a), the reconfiguration of Sb_2S_3 through the CW laser irradiation in the FQ region is illustrated, and an optical microscope image after the laser crystallization is presented in Fig. 5(b). In laser crystallization, a 532 nm CW laser was applied at 2 mW power with a beam size of $3 \mu\text{m}$. In Figs. 5(c) and 5(d) of the Raman characterization excited at 785 nm laser, the original FQ and laser-induced crystalline Sb_2S_3 are observed. The former displays two broadband features, and the latter exhibits crystalline features at 195 , 235 , 280 , and 309 cm^{-1} , indicated by yellow dashed lines. The Sb peak is at 147 cm^{-1} . However, characterization of the IC state was challenging with the Raman spectroscopy based on the optical microscope, as the intermediate region's size was comparable to the beam diameter. In contrast, nano-FTIR enabled the quantitative evaluation of the CW-laser-induced three distinct states of Sb_2S_3 , which will be discussed next.

Fig. 6 shows the nano-FTIR imaging of the CW-laser-induced crystallization (LC) shown in Fig. 5. As shown in Fig. 6(a), the AFM image displays the location of CW-laser irradiation, where the irradiated spot is on the left side. Other results are shown in Figure S7. Figs. 6(b), 6(c), and 6(d) show the hyperspectral images at $900\text{--}1100 \text{ cm}^{-1}$, $1100\text{--}1200 \text{ cm}^{-1}$ and $1200\text{--}1300 \text{ cm}^{-1}$, respectively. While the $900\text{--}1100 \text{ cm}^{-1}$ and $1200\text{--}1300 \text{ cm}^{-1}$ ranges do not clearly differentiate the three states, the image of $1100\text{--}1200 \text{ cm}^{-1}$ range can differentiate them. The nano-FTIR spectra shown in Fig. 6(e) are taken from Fig. 6(c), and they essentially support the observation from the image shown in Fig. 6(c), where the LC area has the highest intensity, followed by the IC and FQ areas. The sequential progression of LC, IC, and FQ states corresponds to the permittivity behavior with distinguished intensities, exhibiting the same characteristics as those observed in Figs. 3 and 4. The spectra are numerically modeled as shown in Figure S1. The fact that the numerical spectra qualitatively reproduce the measured spectra validates the measurements. In Fig. 6(f), line scans across the LC, IC, and FQ states are shown, highlighting the distinct intensities of the three states resulting from the crystallization process. The LC states have intensities greater than 0.60, the IC states range from 0.60 to 0.53, and the FQ states exhibit intensities below 0.53.

Although the advantages of nano-FTIR characterization have been presented, it is constrained by the tip radius, which is typically on the order of tens of nanometers, making atomic-scale analysis impossible. Nevertheless, nano-FTIR is a powerful tool for characterizing chemical states in regions of tens of nanometers or larger, as demonstrated in the current work. In the case of Sb_2S_3 , selecting a specific wavenumber range proved helpful for identifying phase changes. As the suitable range depends on PCM, choosing the appropriate range is the key to nano-FTIR characterization. It is anticipated that using nano-FTIR on other PCMs will provide deeper, higher-resolution insights into phase changes, facilitating the advanced applications of PCMs in reconfigurable photonic devices.

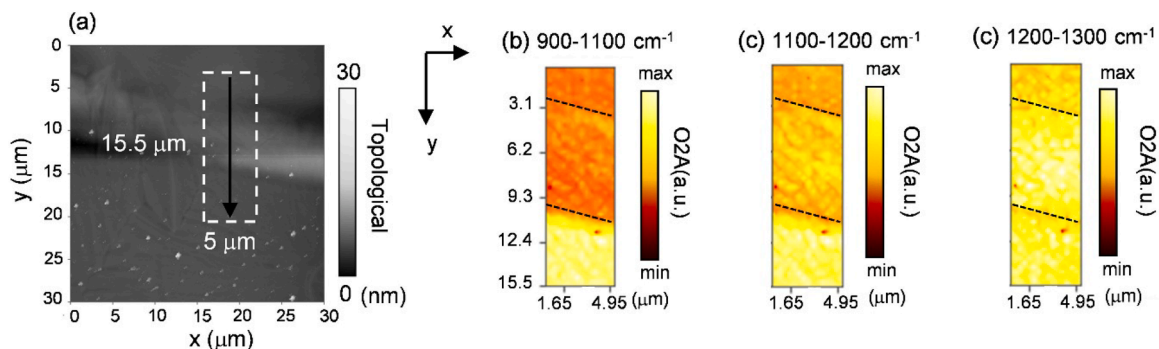


Fig. 4. (a) Topography of the Sb_2S_3 with the white frame and scan arrow indicating the hyperspectral imaging and line scan, respectively. Hyperspectral images of O2A at (b) $900\text{--}1100 \text{ cm}^{-1}$, (c) $1100\text{--}1200 \text{ cm}^{-1}$, and (d) $1200\text{--}1300 \text{ cm}^{-1}$. The resolution is $0.33 \times 0.31 \mu\text{m}^2$ per pixel with a scanning area of $5 \times 15.5 \mu\text{m}^2$.

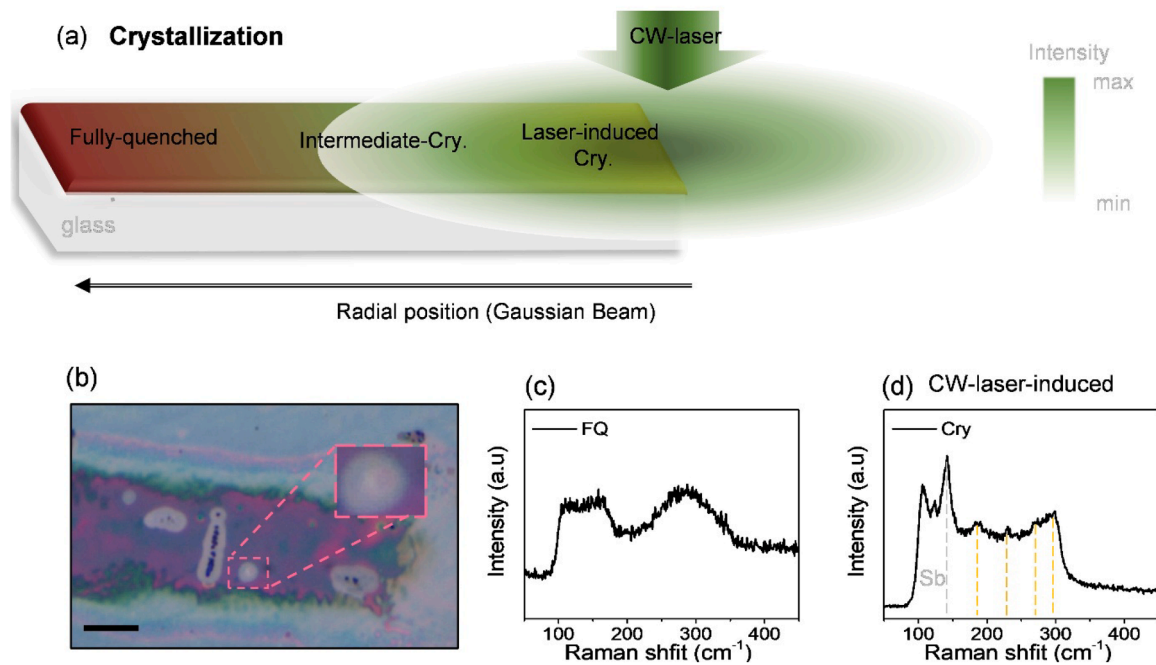


Fig. 5. (a) Schematic of CW-laser-induced heating process with a Gaussian beam irradiated on the device. (b) Optical microscope image of c- Sb_2S_3 /10 nm ITO/glass after crystallization. The scale bar is 10 μm . Raman spectra of Sb_2S_3 taken at (c) an amorphous region and (d) a crystallization region.

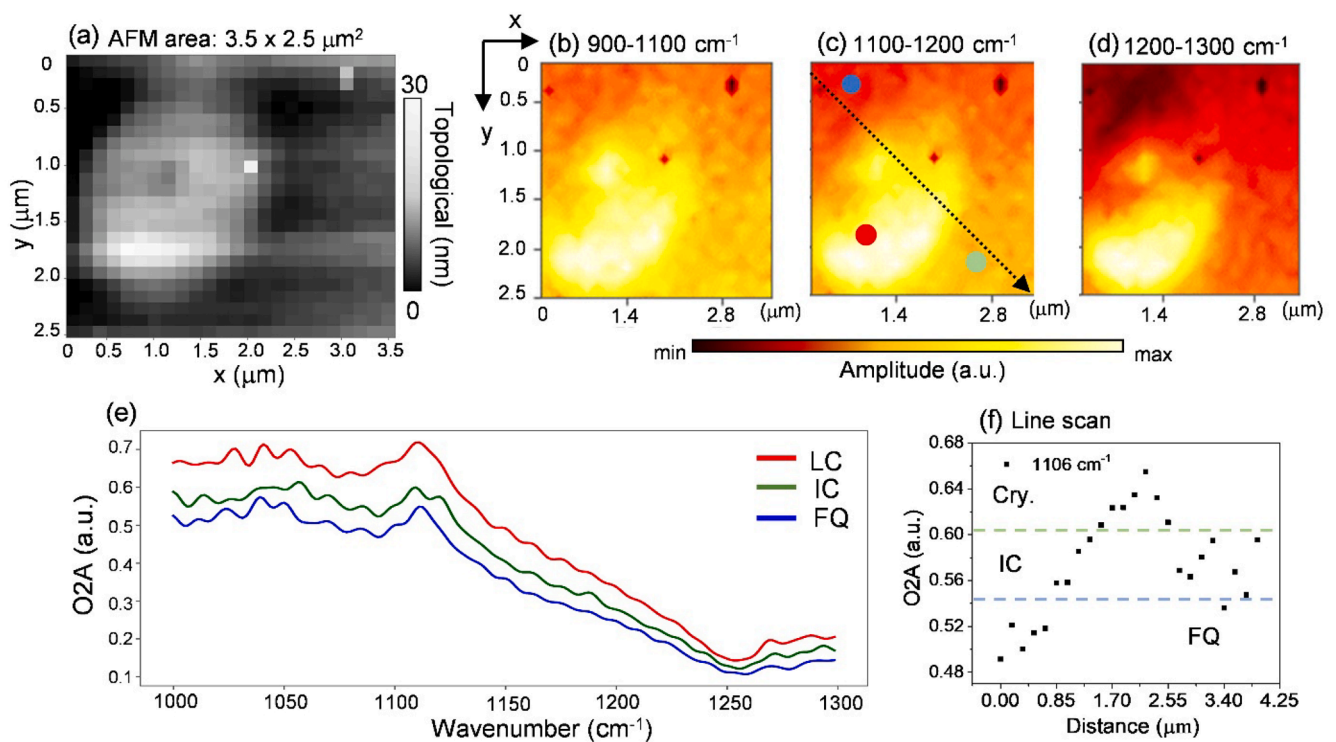


Fig. 6. (a) Topography of Sb_2S_3 after the CW-laser-induced crystallization. Hyperspectral imaging of O2A at (b) 900–1100 cm^{-1} , (c) 1100–1200 cm^{-1} , and (d) 1200–1300 cm^{-1} . The imaging resolution is $0.14 \times 0.1 \mu\text{m}^2$ per pixel. (e) Point scans from the three different states shown in panel (c). (f) Line scans across LC, IC, and FQ states, where the scan direction is shown in a dashed arrow in panel (c).

Conclusions

In this work, the femtosecond laser-induced amorphization and CW laser-induced crystallization of Sb_2S_3 thin films deposited by e-beam evaporation were studied by Raman spectroscopy and nano-FTIR. Using nano-FTIR, we quantitatively distinguish three distinct

states—crystalline, IC, and FQ—which is difficult with Raman spectroscopy owing to its limited spatial resolution. We demonstrate that only the wavenumber range where there is a strong wavenumber-dependence in permittivity (1100–1200 cm^{-1}) can provide clear spatial resolution of these states in nano-FTIR. This study demonstrates that nano-FTIR is a valuable tool for characterizing the phase transitions

of Sb₂S₃, providing critical insights for the design of advanced, reconfigurable photonic devices. Our results pave the way for the development of optical components with enhanced performance and reliability through controlled nanoscale phase transitions.

Methods

Optical characterization

The refractive index and extinction coefficient were collected by an infrared spectroscopic ellipsometer (SENDIRA, SENTECH Instruments GmbH). The Raman spectra were measured by WITec alpha300 (WITec, GmbH, Germany) with a 785 nm CW laser and a 100× (NA = 0.9) objective lens (integration time 10 s, accumulation 1 cycle). The laser power and beam diameter were 1.6 mW and 4.5 μm, respectively. For Raman spectroscopy, both amorphization and crystallization were measured at least three times.

The nano-FTIR was performed using a neaSCOPE (attocube systems GmbH) with a Pt-coated tip of 35 nm radius (NSG 30/Pt). For hyperspectral imaging and line scan, amorphizations were measured at least twice. Crystallization was measured once with an amorphous region. The following conditions were used: an averaging of 3~4 ms integration time, a 0.14×0.1 μm² area resolution (scan area 3.5 × 2.5 μm²), and a tapping amplitude of 65.49 nm for crystallization. An averaging of 4~5 ms integration time, 0.31×0.31 μm² area resolution (scan area 5 × 15.5 μm²), and tapping amplitude 56.79 nm for amorphization.

Laser-induced phase change

For the amorphization, a femtosecond laser system (Spectra-Physics) equipped with an optical parametric amplifier was used. The laser beam had a wavelength of 532 nm, a pulse duration of approximately 100 fs, a repetition rate of 1 kHz, an average power of 1.6 mW, and a one-directional sweep rate of 50 μm/s. The laser beam was focused by an objective lens (PL LWDM40X; 40×, NA = 0.5).

CRedit authorship contribution statement

Ming-Jyun Ye: Writing – review & editing, Writing – original draft, Visualization, Validation, Methodology, Investigation, Formal analysis, Data curation, Conceptualization. **Ilario Bisignano:** Validation, Formal analysis. **Ross Y.M. Wong:** Formal analysis. **Hung-Wen Chen:** Writing – review & editing, Conceptualization. **Yoshihiko Takeda:** Resources, Methodology. **Kuo-Ping Chen:** Writing – review & editing, Visualization, Validation, Supervision, Resources, Formal analysis, Conceptualization. **Satoshi Ishii:** Writing – review & editing, Visualization, Validation, Supervision, Resources, Methodology, Formal analysis, Data curation.

Declaration of competing interest

The authors declare that they have no known competing financial interests or personal relationships that could have appeared to influence the work reported in this paper.

Acknowledgment

This work is supported by JST FOREST (JPMJFR2139), the National Science and Technology Council (NSTC 112–2223-E-007-007-MY3; 114–2112-M-007–037). M.J.Y. acknowledges the International Collaborative Graduate Program supported by NIMS. The support from Taiwan Semiconductor Research Institute (TSRI) and the Center for Nanotechnology, Materials Science and Microsystems (CNMM), NTHU is highly appreciated.

Supplementary materials

Supplementary material associated with this article can be found, in the online version, at doi:10.1016/j.apsadv.2026.101000.

Data availability

Data will be made available on request.

References

- [1] R. Chen, Z. Fang, C. Perez, F. Miller, K. Kumari, A. Saxena, J. Zheng, S.J. Geiger, K. E. Goodson, A. Majumdar, Non-volatile electrically programmable integrated photonics with a 5-bit operation, *Nat. Commun.* 14 (2023) 3465.
- [2] H. Liu, W. Dong, H. Wang, L. Lu, Q. Ruan, Y.S. Tan, R.E. Simpson, J.K. Yang, Rewritable color nanoprins in antimony trisulfide films, *Sci Adv.* 6 (2020) eabb7171.
- [3] P. Li, X. Yang, T.W. Maß, J. Hanss, M. Lewin, A.K.U. Michel, M. Wuttig, T. Taubner, Reversible optical switching of highly confined phonon–polaritons with an ultrathin phase-change material, *Nat. Mater.* 15 (2016) 870–875.
- [4] K. Chaudhary, M. Tamagnone, X. Yin, C.M. Spägle, S.L. Oscurato, J. Li, C. Persch, R. Li, N.A. Rubin, L.A. Jauregui, Polariton nanophotonics using phase-change materials, *Nat. Commun.* 10 (2019) 4487.
- [5] H. Sumikura, T. Wang, P. Li, A.K.U. Michel, A. Heßler, L. Jung, M. Lewin, M. Wuttig, D.N. Chigrin, T. Taubner, Highly confined and switchable mid-infrared surface phonon polariton resonances of planar circular cavities with a phase change material, *Nano Lett.* 19 (2019) 2549–2554.
- [6] C. Chen, S. Chen, R.P. Lobo, C. Maciel-Escudero, M. Lewin, T. Taubner, W. Xiong, M. Xu, X. Zhang, X. Miao, Terahertz nanoimaging and nanospectroscopy of chalcogenide phase-change materials, *ACS Photon.* 7 (2020) 3499–3506.
- [7] Y. Canvel, S. Lagrasta, C. Boixaderas, S. Barnola, Y. Mazel, E. Martinez, Study of Ge-rich GeSbTe etching process with different halogen plasmas, *J. Vac. Sci. Technol. A* 37 (2019).
- [8] G. Lama, M. Bernard, G. Bourgeois, J. Garrione, V. Meli, N. Castellani, C. Sabbione, L. Prazakova, D.S.F. Rodas, E. Nolot, Multilayered Sb-rich GeSbTe phase-change memory for best endurance and reduced variability, *IEEE Trans. Electron. Dev.* 69 (2022) 4248–4253.
- [9] S. Guerin, B. Hayden, D.W. Hewak, C. Vian, Synthesis and screening of phase change chalcogenide thin film materials for data storage, *ACS Comb. Sci.* 19 (2017) 478–491.
- [10] K. Gao, K. Du, S. Tian, H. Wang, L. Zhang, Y. Guo, B. Luo, W. Zhang, T. Mei, Intermediate phase-change states with improved cycling durability of Sb₂S₃ by femtosecond multi-pulse laser irradiation, *Adv. Funct. Mater.* 31 (2021) 2103327.
- [11] T.Y. Teo, M. Krbal, J. Mistrik, J. Prikrýl, L. Lu, R.E. Simpson, Comparison and analysis of phase change materials-based reconfigurable silicon photonic directional couplers, *Opt. Mater. Express.* 12 (2022) 606–621.
- [12] P. Moitra, Y. Wang, X. Liang, L. Lu, A. Poh, T.W. Mass, R.E. Simpson, A. I. Kuznetsov, R. Paniagua-Dominguez, Programmable wavefront control in the visible spectrum using low-loss chalcogenide phase-change metasurfaces, *Adv. Mater.* 35 (2023) 2205367.
- [13] M.J. Ye, R.G. Bikbaev, P.S. Pankin, L.H. Chen, D. Chiu, I.V. Timofeev, H.W. Chen, S. Ishii, K.P. Chen, Lossless phase change materials for adjustable tamm plasmon polaritons in the near-infrared, *Adv. Opt. Mater.* (2025) 2402889.
- [14] A. Yang, M. Sun, H. Ren, H. Lin, X. Feng, Z. Yang, Dy³⁺-doped Ga₂S₃-Sb₂S₃-La₂S₃ chalcogenide glass for mid-infrared fiber laser medium, *J. Lumin.* 237 (2021) 118169.
- [15] M. Ichikawa, Y.I. Ishikawa, T. Wakasugi, K. Kadono, Mid-infrared emissions from Ho³⁺ in Ga₂S₃-GeS₂-Sb₂S₃ glass, *J. Lumin.* 132 (2012) 784–788.
- [16] H. Wang, L. Wang, D.S. Jakob, X.G. Xu, Tomographic and multimodal scattering-type scanning near-field optical microscopy with peak force tapping mode, *Nat. Commun.* 9 (2018) 2005.
- [17] L. Mester, A.A. Govyadinov, S. Chen, M. Goikoetxea, R. Hillenbrand, Subsurface chemical nanoindentification by nano-FTIR spectroscopy, *Nat. Commun.* 11 (2020) 3359.
- [18] C. Laprais, C. Zrounba, J. Bouvier, N. Blanchard, M. Bugnet, A. Gassenq, Y. Gutiérrez, S. Vazquez-Miranda, S. Espinoza, P. Thiesen, Reversible single-pulse laser-induced phase change of Sb₂S₃ thin films: multi-physics modeling and experimental demonstrations, *Adv. Opt. Mater.* 12 (2024) 2401214.
- [19] A. Cvitkovic, N. Ocelic, R. Hillenbrand, Analytical model for quantitative prediction of material contrasts in scattering-type near-field optical microscopy, *Opt. Express.* 15 (2007) 8550–8565.
- [20] L. Lu, Z. Dong, F. Tijptoharsono, R.J.H. Ng, H. Wang, S.D. Rezaei, Y. Wang, H. S. Leong, P.C. Lim, J.K. Yang, Reversible tuning of Mie resonances in the visible spectrum, *ACS Nano.* 15 (2021) 19722–19732.
- [21] R. Parize, T. Cossuet, O. Chaix-Pluchery, H. Roussel, E. Appert, V. Consonni, In situ analysis of the crystallization process of Sb₂S₃ thin films by Raman scattering and X-ray diffraction, *Mater. Des.* 121 (2017) 1–10.

- [22] Y. Liu, K.T.E. Chua, T.C. Sum, C.K. Gan, First-principles study of the lattice dynamics of Sb₂S₃, *Phys. Chem. Chem. Phys.* 16 (2014) 345–350.
- [23] P. Sereni, M. Musso, P. Knoll, P. Blaha, K. Schwarz, G. Schmidt, Polarization-dependent Raman characterization of stibnite (Sb₂S₃), in: *AIP Conference Proceedings*, American Institute of Physics, 2010, pp. 1131–1132.
- [24] A. Caldiroli, S. Cappelletti, G. Birarda, A. Redaelli, S.A. Riboldi, C. Stani, L. Vaccari, F. Piccirilli, Infrared nanospectroscopy depth-dependent study of modern materials: morpho-chemical analysis of polyurethane/fibroin binary meshes, *Analyst* 148 (2023) 3584–3593.